Arabian Journal of Chemistry (2022) **15**, 103944

King Saud University

Arabian Journal of Chemistry

www.ksu.edu.sa
www.sciencedirect.com

ORIGINAL ARTICLE

Facile fabrication of steam-exploded poplar loaded with non-metal-doped Ni-Fe nanoparticles: Catalytic activities in 4-nitrophenol reduction and electrocatalytic reaction

Cheng Pan *, Guangying Yang, Haitao Yang, Lei Wang, Jungang Jiang, Yifan Zhang, Feifan Wu

Hubei Provincial Key Laboratory of Green Materials for Light Industry, Hubei University of Technology, Wuhan, China

Received 24 February 2022; accepted 1 May 2022
Available online 10 May 2022

KEYWORDS

Steam exploded poplar;
Ni-Fe nanoparticles;
Catalytic hydrogenation

Abstract A simple and effective method for preparing a non-metallic ion-doped nickel-supported catalyst is reported. Using economical and recyclable fibre raw materials as carriers, nickel-supported catalysts were prepared by adsorption and reduction at room temperature. The nanoparticles dispersed and anchored on a rational support, efficiently inhibiting their aggregation and thus enhancing the catalytic activity. For the model catalytic hydrogenation of 4-nitrophenol by $NaBH_4$, the N-B-NiP/steam-exploded poplar (SEP) and N-B-Ni_5Fe_5P/SEP catalysts exhibited much better catalytic performances than the other recently reported catalysts in terms of the catalytic activity (the reaction was completed within 10 min for both aforementioned catalysts), reaction rate constant (0.19 and 0.344 min^{-1}, respectively) and the activity factor K (19 and 34.4 $min^{-1}{\cdot}g^{-1}$, respectively). The catalysts showed activities for electrocatalytic hydrogen evolution reaction (HER) and oxygen evolution reaction (OER) under ambient conditions. In general, the reported preparation method of nickel-supported catalysts is convenient, economical and environment-friendly, and is agreement with many green chemistry and sustainable development principles; further, it employs widely available starting materials.

1. Introduction

To tackle the problems of energy crisis and environmental pollution, clean and renewable energy sources are required to replace the fossil fuels widely used to generate electricity. As an alternative energy sources, hydrogen is becoming an important part of the future energy system because of its high energy density and environment-friendliness. In recent years,

* Corresponding author.
E-mail address: ch_pan1018@hbut.edu.cn (C. Pan).
Peer review under responsibility of King Saud University.

Production and hosting by Elsevier

https://doi.org/10.1016/j.arabjc.2022.103944
1878-5352

hydrogen production by hydrolysis has garnered attention worldwide as an economic and feasible method. At present, the development of catalysts with high hydrolysis efficiency is an unresolved issue; various rare-earth-rich non-precious metal catalysts containing transition metal compounds such as sulfides, phosphates, carbides, nitrides, oxides and selenides have been developed (Chang et al., 2016). The addition of non-metallic elements (O, S or N) to the transition metal-based electrocatalyst can also adjust the kinetics of the reaction and improve the catalytic activity (Xu et al., 2017; Hao et al., 2017; Anjum et al., 2018).

As yet, nickel-supported catalysts were used for hydrogenation, oxygen reduction and olefin oxidation of nitrobenzene and nitrophenol; these catalysts have attracted interest because of their low cost and excellent catalytic performance. To facilitate catalysts recovery, nickel particles are usually dispersed in a solid matrix. Recently, much efforts were made to prepare heterogeneous nickel catalysts using various materials such as silica (Mitchell et al., 2021), alumina, graphene/amorphous carbon (Sung et al., 2018), zirconia (Wojciech Gac, et al., 2020), titanium dioxide (Jiang, et al., 2017.), magnesia (Yusuf et al., 2021) and carbon. Among them, porous carbon is the most commonly used economic carrier, and carbon-based carriers such as cellulose paper with metallic nickel particles chemically deposited on the surface (Sahasrabudhe et al., 2018), nickel based mesoporous carbons (Yang et al., 2014), in situ prepared of Ru nanoclusters and porous carbon (Ding R et al., 2020b) have many advantages over other carriers because of their chemical inertia and stability. Compared with other carbon materials, the advantages of carbonised fibre obtained from biomass include easier availability, easier regeneration and lower cost (Lai et al., 2019).

Meanwhile, the gradual shift of technology towards green synthetic strategy has necessitated the use of nontoxic, renewable and environmentally benign chemicals (Zhou et al., 2018; Kuo et al., 2019). Hence, designing high-value products with long life, reusability, cost-effectiveness and high efficiency has become an urgent need. Unfortunately, the products of agricultural, industrial or forestry wastes are complex and difficult to separate. Therefore, one of the great challenges in the preparation of biological carriers is to transform them into specific products with specific properties and complexity. Other complex factors include excessive accumulation of chemicals during the use of the product, natural ageing, the recycling process itself and the flow of materials and products associated with it (Kümmerer et al., 2020). However, these biomass catalysts are mostly powders with small particle size. To solve the problem of small particle size of carbon-based solids, nickel-supported catalysts were prepared from poplar with the original skeleton structure. Carbonised wood has the potential to be used as catalyst carrier owing to its good microstructure. Poplar wood has the advantages of low weight, long fibres, high content and easy processing, and hence, it is widely used in housing and as pulp and plywood. Poplar is widely grown because of its fast-growing nature and huge carbon emission reduction potential. It is regarded an important industrial raw material in many countries and its use as an energy crop for biomass or biofuel is gaining interest.

Steam explosion is an optional and mature pretreatment technology in the field of biomass conversion. The effect of this technology on hardwood is second only to that on gramineous plants. Since most gramineous plants are a part of crop waste, and the sampling time is greatly affected by seasons, researchers focused on poplar among the perennial broad-leaved trees. The particle sizes of different types of biological raw materials differ after steam blasting. In the process of the steam explosion treatment of biomass raw materials, a large amount of water vapour permeates into raw biomass materials, resulting in the formation of hydrogen bonds with some hydroxyl groups on the cellulose molecular chain. In addition, high temperature and high pressure exacerbate the fracture of the hydrogen bond in cellulose and cause the release of new hydroxyl groups; the specific surface area of cellulose increases and the adsorption capacity of blasting products is improved. Because lignocellulose is renewable and rich in hydroxyl groups, it is an ideal carbon source for preparing carbon carriers. During the preparation process, embedding the nickel nanoparticles directly into carbon materials is crucial for preparing 'embedded' catalysts.

Herein, we report a simple and effective method for preparing a non-metallic ion-doped nickel-supported catalyst using economical and recyclable fibre raw materials as carriers. The nickel-supported catalysts were prepared by adsorption and reduction at room temperature; among the catalysts, non-metallic ions and Ni-Fe metal particles are highly dispersed. The nanoparticles dispersed and anchored on a rational support can efficiently inhibit the aggregation and thus enhance the catalytic activity (Fu et al., 2019a). Non-metallic ion-doped nickel-supported catalysts exhibited catalytic activity and durability, and can be used in various catalytic reactions, such as electrochemical reactions, 4-nitrophenol (4-NP) reduction and so on. In general, the reported preparation method of the nickel-supported catalyst is convenient, economic and environment-friendly, which is in line with many green chemistry and sustainable development principles and employs widely available starting materials.

2. Experimental materials

Poplar was steam exploded at 213 °C for 5 min. A compositional analysis of steam exploded poplar (SEP) on a dry basis was performed. Analytical grade hydrogen sodium borohydride ($NaBH_4$) and 4-NP were procured from Sigma-Aldrich (Shanghai, China). Nickel nitrate hexahydrate, iron nitrate nonahydrate and ethanol were analytical grade and procured from Sinopharm Chemical Reagent Co., Ltd. (Shanghai, China). All chemicals were used without further purification.

3. Nickel supported catalyst preparation

SEP was prepared at 213 °C for 5 min by steam explosion. First, 2 g SEP and Nickel nitrate hexahydrate (5 mmol) were dispersed in 100 mL of deionised water for 15 min under ultrasonic treatment, and stirred for 40 min to completely dissolve. After Ni^{2+} was completely adsorbed by the SEP, 5 mL of $NaBH_4$ (0.5 mol/L) solution was added, and the boron-containing metal oxide was grown vertically in situ in the SEP at room temperature. The resulting product was collected by centrifugation and washing with deionised water and ethanol, and then dried overnight in vacuo. The obtained carbon material is hereafter referred to as N-B-Ni/SEP. Thereafter, the obtained product was used to pyrolyse the feedstock as fol-

lows: the precursor and 200 mg NaH_2PO_2 will be prepared at both ends of the alumina crucible. Temperature was increased at a rate of 5 °C/min in a nitrogen atmosphere, and the N-B-Ni/SEP was held for 1.5 h at 350 °C, followed by cooling to room temperature inside the furnace. The carbon material obtained thus is hereinafter referred to as N-B-NiP/SEP. N-B-Ni_5Fe_5P/SEP was prepared by adding nickel nitrate hexahydrate (5 mmol) and iron nitrate nonahydrate (5 mmol), under identical conditions as described in the previous sentences.

4. Characterization

A Fourier transform infrared (FT-IR) spectrometer (Karlsruebrook, Germany) using KBr pellet technology was employed to measure FT-IR. A Zeiss Merlin instrument was used for scanning electron microscopy (SEM) under 10 kV voltage. Energy dispersive spectroscopy (EDS) was performed to determine the elemental composition. The crystal structure of the sample was analyzed by using an Ultima IV X-ray diffractometer. The working voltage of the X-ray diffractometer was 40 kV, and the current density was 30 mA. X-ray photoelectron spectroscopy (XPS) analysis was carried out by using an ESCALAB 250 analyzer (Thermo Science) and a monochromatic Al Ka X-ray source. Raman spectroscopy (Horiba evolution) measurements were employed to study the physical properties of the samples. The adsorption–desorption isotherms of nitrogen were determined using a BELSORP-mini II instrument and the Brunauer-Emmett-Teller (BET) method. The ultraviolet (UV)- visible (vis) absorption spectra were recorded via a UV-2900 spectrophotometer (Hitachi, Japan). Inductive coupling plasma emission spectroscopy (ICP-OES) was performed using a PerkinElmer 8300 analyzer.

5. Catalytic reduction of 4-NP

The reduction of 4-NP was performed in a quartz cuvette and monitored by performing UV–vis spectroscopy (Hitachi UV-2900) at room temperature. For comparison, an aqueous 4-NP solution (0.01 M) was prepared and measured prior to monitoring the change in absorption. Then, a total of 25 µl of aqueous 4-NP solution was mixed with 2.5 mL of fresh $NaBH_4$ (0.01 M) solution. Subsequently, a fixed amount of nickel catalyst was added to start the reaction, and UV spectrometry was employed to monitor the reduction in situ by measuring the absorbance of the solution at 400 nm over time.

6. Electrochemical characterization

The electrochemical measurement was carried out at room temperature using a three-electrode device using CHI760E electrochemical workstation. A glassy carbon electrode was the working electrode (opposite electrode), and the Ag/AgCl electrode was the reference electrode. The linear sweep voltammogram (LSV) was recorded at a scanning rate of 5 mV/s in 1.0 M KOH electrolyte for OER, and in 0.5 M H_2SO_4 for HER. The scanning range was 1.0–1.8 vs. reversible hydrogen electrode (RHE). The LSV curve was obtained at a scanning rate of 5 mV/s, and the LSV curve was corrected by 90% IR compensation method. Using the Nernst equation ($E_{RHE} = E_{Ag/AgCl} + 0.059 \cdot pH + 0.197$), the measured potential was converted into the corresponding RHE potential. The current density (J) was normalized to the geometric surface area, and the measured potential E_{Appl} (vs. Ag/AgCl) was converted into the RHE. The overpotential (η) of OER when the current density was 10 mA/cm^2 was calculated by using the equation $\eta = E_{RHE}$-1.23 V. The overpotential (η) of the HER when the current density was 10 mA/cm^2 was calculated using the equation ($\eta = E_{RHE}$). According to the Tafel equation ($\eta = a + b \cdot \log(J)$ to calculate the Tafel slope (b), the Tafel slope was obtained by fitting the linear part of the Tafel curve (Cao et al., 2020; Lan et al., 2019).

7. Results and discussion characterizations

The FT-IR analyzer was used to identify the functional groups on the catalyst samples and SEP surface, as shown in Fig. 1. The FT-IR spectra showed strong absorption at 3421 cm^{-1}, which is attributed to the stretching of the phenolic and aliphatic hydroxyl groups. The peaks at around 2921 cm^{-1} that were related to the C-H functional group changed after the nickel-supported catalyst samples were prepared by the SEP. The results showed that chemical interactions and ion changes occurred between OH, C–H, C=O and heavy metal ions in the nickel bio-adsorption process (Foroutan et al., 2019b). The FT-IR spectra of N-B-NiP/SEP, N-B-Ni_5Fe_5P/SEP and N-B-Ni_5Fe_5P/SEP-1 confirmed the existence of NO_3^- and OH^- group in the nickel–iron loaded catalyst (Fig. 2). The bands at 1596, 1363 and 777 cm^{-1} were the characteristic vibrations for H_2O, $-NO_3^-$and Metal-O (M–O) (Lee et al. 2019; Yang et al. 2019), respectively, thereby showing again that Ni-Fe formed on SEP. Compared with the blank SEP, the change in the absorption peak at 777 cm^{-1} indicated that metal particles were attached to the surface of SEP. In contrast, the weak peaks at 1112 cm^{-1} are characteristic of the C-N stretching mode (Coates 2006). The absorption peaks of the repeatedly used catalysts at 777 cm^{-1} did not diminish, indicating that the catalytic process did not affect the transition metal particles on the carrier surface.

The morphology and microstructural information of the N-B-Ni_5Fe_5P/SEP and N, B-NiP/SEP were systematically studied using electron microscopy techniques (Xiao et al., 2016). The closely packed Ni-Fe coating deposited at room temperature did not change the fibre structure of the SEP (Fig. 3a-b). The nickel-plated iron or nickel SEM contain a large number of voids in the bracket. SEM images (Fig. 3a-b) show that the growth of the Ni-Fe layer with vertically arranged nano-thin sheets, with interconnected macroporous morphology, will not hinder the underlying macroporous structure. This interesting morphology is beneficial for electrocatalysis because it provides a large number of exposed catalytic active sites and enables electrons to travel rapidly along vertical nanoflakes. Energy dispersive X-ray (EDX) spectroscopy was performed to further characterize the elemental composition and distribution of the N-B-Ni_5Fe_5P/SEP sample by performing EDS surface scans (Fig. 3d-g). The results show that Ni, Fe, P, B and N are uniformly distributed in the sample, and that the atomic ratio is 1.28 (Ni): 1.21 (Fe). Further, B and N atoms were confirmed to have successfully entered the SEP. The above results further prove that the N-B-Ni_5Fe_5P/SEP was successfully realized by introducing zero-valent N and B atoms.

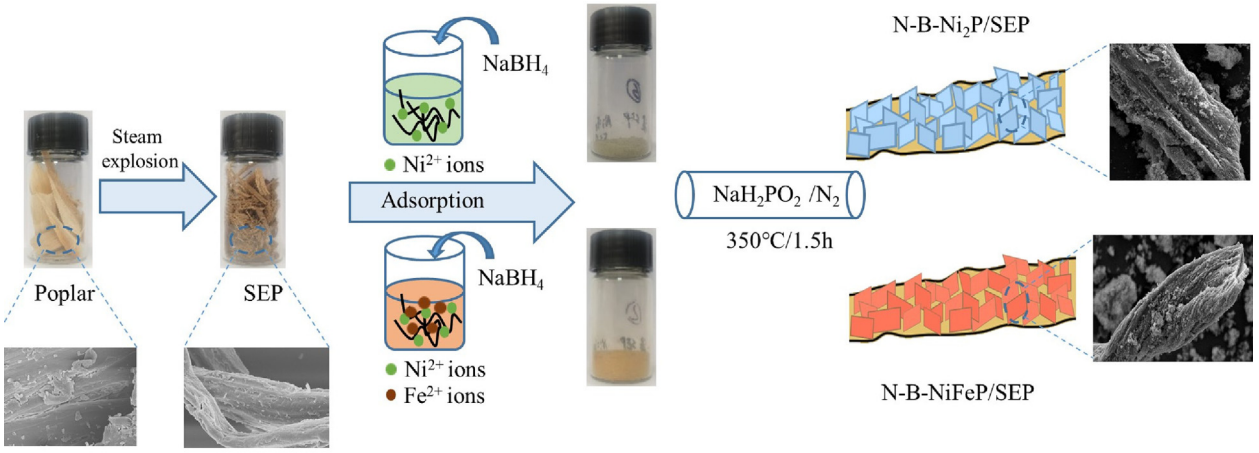

Fig. 1 Schematic representation for the prepared process of N-B-NiP/SEP and N-B-Ni_5Fe_5P/SEP.

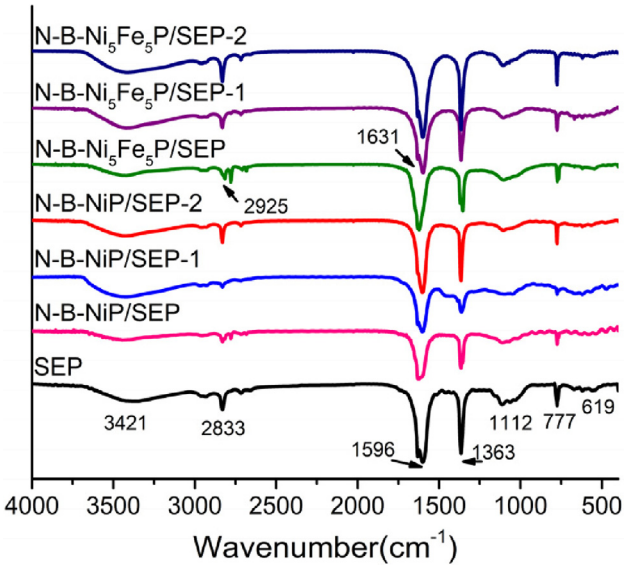

Fig. 2 FT-IR spectra of SEP, N-B-NiP/SEP, N-B-Ni_5Fe_5P/SEP and N-B-Ni_5Fe_5P/SEP-1.

The detailed structural features of the obtained sample were first investigated by an X-ray diffraction (XRD) study. All the diffraction peaks were ascribed to the hexagonal NiP (JCPDS card No. 03-065-1989) without any peaks for impurities, suggesting that the N-B-NiP/SEP precursor was successfully converted into nickel phosphide/SEP. (Pinilla et al., 2016; Sun et al., 2020). The diffraction pattern for PC has a broad peak at 26°, which is a characteristic of the (0 0 2) plane of graphitic carbon (Fig. 4).

Compared with N-B-NiP/SEP, the four diffraction peaks of NiP in the XRD spectrum of the Fe-doped catalyst (N-B-Ni_5Fe_5P/SEP) shifted to a larger diffraction angle with Fe doping, indicating that Fe atoms enter the Ni lattice to form an Fe-Ni alloy. The intensity of the diffraction peaks of 111, 201, 210 and 300 of Ni decreases with Fe doping, indicating that Fe doping affects the crystallinity of the alloy particles.

The average crystallite size was determined to be about 10.78 nm for N-B-Ni_5Fe_5P/SEP, and 17.97 nm for N-B-NiP/SEP from the (1 1 1) reflection by utilizing Scherrer's equation that relates the coherently scattering domains with Bragg peak widths: $D = k\lambda/B\cos(\theta)$, where $k = 0.89$ for spherical particles, and B is the full angular width at half-maximum of the peak in radians. Combined with the aforementioned energy spectrum (Fig. 3d-g), it can be seen that the Ni-Fe elements are uniformly distributed on the carrier surface. From these results, we come to the conclusion that the metal particles are well dispersed on the fibre surface, and Fe doping affects the crystallinity of the alloy particles. The above results show that the addition of Ni can effectively promote the miniaturization of Fe grains (Mansouriieh et al., 2016). The XRD pattern of Ni_5Fe_5/Ni-P electrode (Fig. 4) further confirms the amorphous nature of Ni-Fe catalyst layer as no new peaks are observed besides those corresponding to the catalyst. In fact, it has been proposed that amorphous Ni-Fe electrocatalysts are much more active than their crystalline counterparts because the amorphous electrocatalysts have good structural flexibility and high density of co-ordinatively unsaturated sites that help in the adsorption of oxidized intermediates.

The XPS survey scan spectrum (Fig. 5a) clearly confirmed that Ni, Fe, B, P, N, O, and C elements were present in the samples. According to the XPS analysis, the Ni and Fe contents in N-B-Ni_5Fe_5P/SEP were 11.14 and 14.84 wt% (Table 1), respectively. The molar ratio and actual total loading content of Fe and Ni in the N-B-Ni_5Fe_5P/SEP and N-B-NiP/SEP catalysts were further determined by ICP-MS, as listed in Table 1. The results are in good agreement with the theoretical molar ratio, indicating that the Ni and Fe metal particles are uniformly dispersed on the SEP carrier. Note that the Ni and Fe loading of N-B-Ni_5Fe_5P/SEP from ICP-OES (17.19 and 15.58 wt%, respectively) analysis were much higher than the outmost surface Ni and Fe content (11.14 and 14.84 wt%, respectively) as measured by XPS. Hence, we conclude that the tiny Ni and Fe particles are embedded in the carbon fibre instead of being anchored on the surface (Ding et al., 2020). This phenomenon is more obvious in the nickel content of the N-B-NiP/SEP.

The high-resolution spectra of the Ni 2p region showed two peaks, 2p3/2 (856.82 eV) and 2p1/2 (874.47 eV) corresponding to the Ni^{2+} derived from the oxidation of the NiP surface (with the corresponding shakeup satellite peaks at 862.26

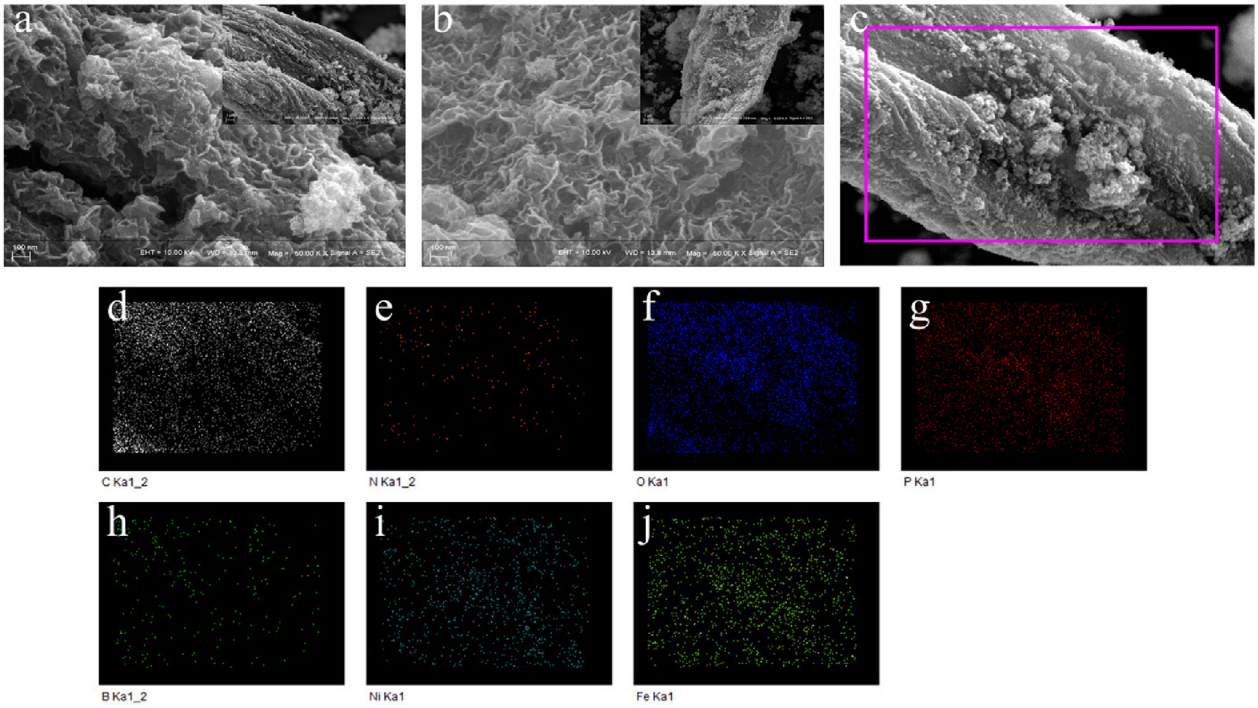

Fig. 3 Morphology, structure and chemical composition analyses of N-B-Ni_5Fe_5P/SEP and N, B-NiP/SEP. (a) SEM images of N-B-Ni_5Fe_5P/SEP, inset is a low-magnification image, (b) SEM images of N, B-NiP/SEP, (c-j) EDS of N-B-Ni_5Fe_5P/SEP.

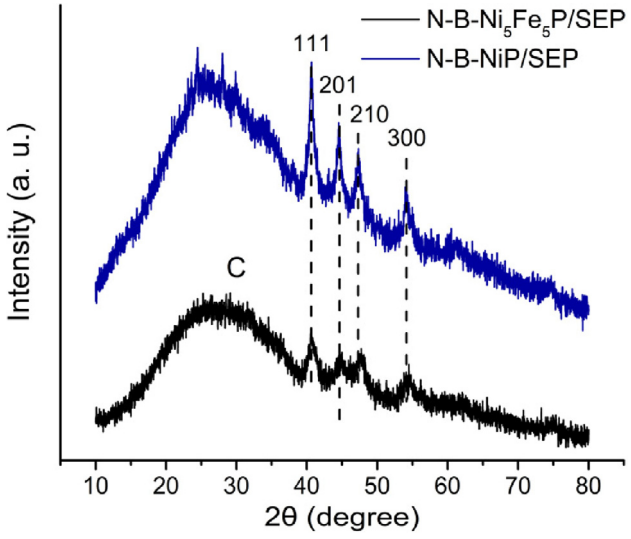

Fig. 4 XRD spectra of N-B-Ni_5Fe_5P/SEP and N-B-NiP/SEP.

and 880.03 eV, respectively) (Ding et al., 2020). The Fe 2p spectrum (Fig. 5h) was fitted into two separate peaks at 711.76 and 724.68 eV corresponding to the spin–orbit states of Fe 2p3/2and Fe 2p1/2, respectively. This finding also confirms that the Fe predominantly exists in the Fe^{3+} state. As shown in Fig. 5g, compared with the N-B-NiP/SEP, the negative shift of NiP indicates a decrease in the number of electrons at Fe site and the accumulation of electrons around the Ni site (Jiao et al., 2019). These changes in electron accumulation cause changes in the distribution of electrons, thus changing the local electronic structure of the metal position.

The XPS spectrum (Fig. 5c) for O 1s of samples can be deconvoluted into two peaks at binding energies of 531.08 and 532.08 eV, which were attributed to the surface-adsorbed water (–OH) and C-O species (oxygen vacancies), respectively. The oxygen vacancies indicate a defect site with low oxygen coordination, which decrease the barrier for the adsorption of OH^- and promotes OER. In particular, N-B-Ni_5Fe_5P/SEP and N-B-NiP/SEP show a clear difference in the area of oxygen vacancies because of the presence of Fe metal ions (29.49 %: 51.62 %) (Xu et al., 2018; Kim et al., 2020).

As shown in Fig. 5b, the four components of C1s spectrum (284.77, 286.36, 288.49 and 291.54 eV) were attributed to sp2 C-C, sp3 C-C, C-O and carboxylic groups, respectively. In the high-resolution XPS spectra, P 2p exhibits three contributions, P 2p3/2 and P 2p1/2, located at 129.49 and 130.46 eV (Fig. 5e), respectively, which are assigned to NiP, and the peak at 133.72 eV that is attributed to the oxidized P species.

The B 1s spectrum (Fig. 5f) clearly evidences the presence of three chemical environments for phosphorus atoms (B-O, B-C, and B-Ni). The existence of B^{3+} in N-B-Ni_5Fe_5P/SEP and N-B-NiP/SEP catalyst is evidenced by the peak at 191.60 eV (Fig. 5f), which can be attributed to the surface oxidation of the borate species. Compared with N-B-NiP/SEP, the peak intensity at 190.59 eV of N-B-Ni_5Fe_5P/SEP that corresponds to B-C bonds was higher, indicating that some C atoms in the carbon fibre were replaced by B atoms. Pleasantly, the peak at 187.33 eV can be attributed to B(0) in the Ni-B bonds, which matches well with the literature. This result suggests that there are abundant zero-valent B atoms in the N-B-Ni_5Fe_5P/SEP and N-B-NiP/SEP after N_2 treatment.

In the high-resolution N 1s spectrum, in addition to the characteristics related to pyrrolic-N (402.07 eV) and

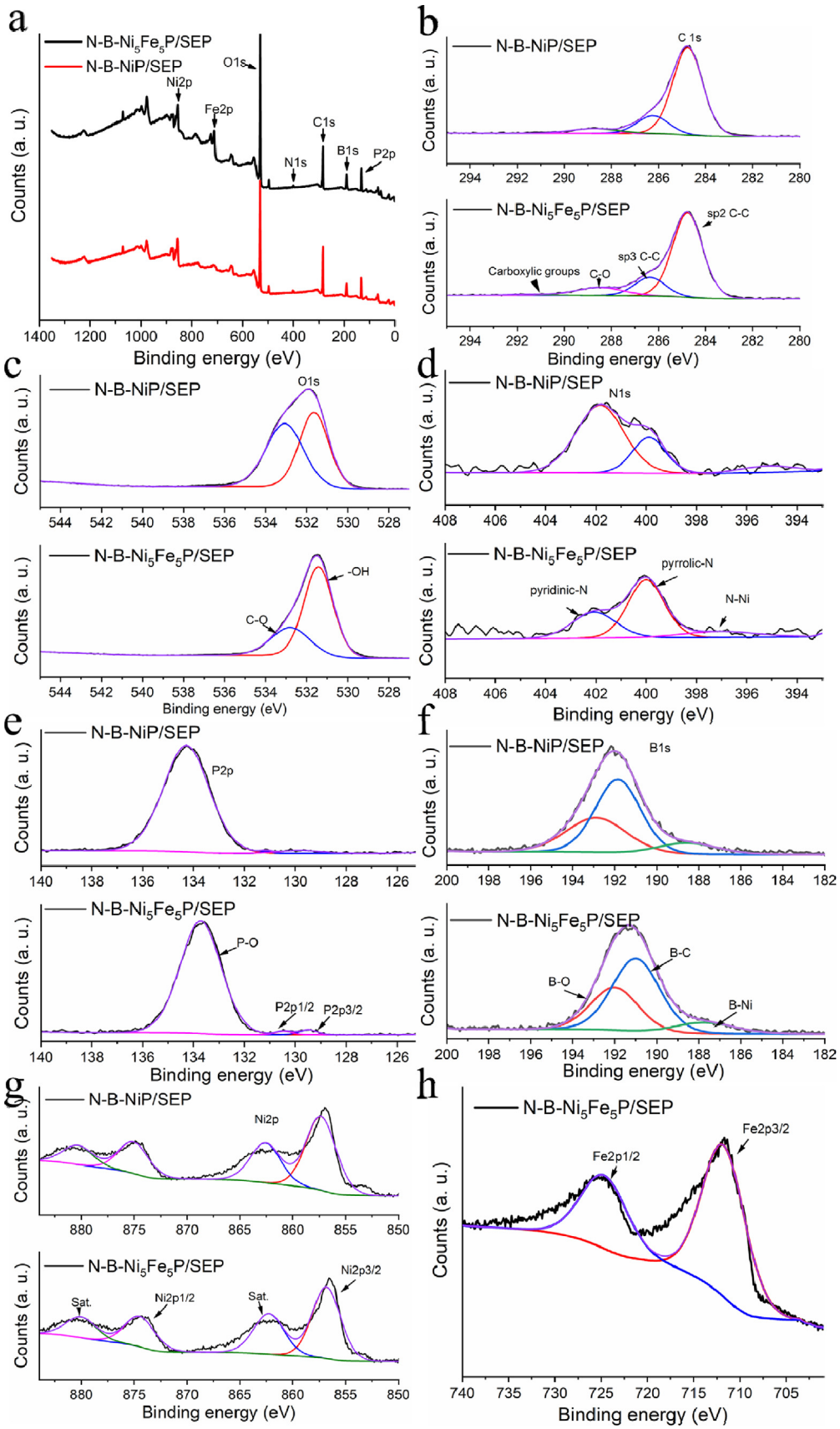

Fig. 5 (a) XPS survey spectrum and (b-h) high-resolution XPS spectra of C1s, O1s, N1s, P2p, B1s, Ni2p, Fe2p of N-B-Ni_5Fe_5P/SEP and N-B-NiP/SEP.

Table 1 Catalysts composition determined by ICP-MS and XPS.

Catalysts	Fe loading (wt%)	Ni loading (wt%)	Fe:Ni (molar ratio)	FeNi loading (wt%)	
N-B-Ni_5Fe_5P/SEP (1:1)	15.58	17.19	1:1.05	32.77	ICP-MS
N-B-NiP/SEP	/	27.71	/	27.71	
N-B-Ni_5Fe_5P/SEP (1:1)	14.84	11.14	1:0.75	25.98	XPS
N-B-NiP/SEP	/	13.88	/	13.88	

pyridinic-N (400.00 eV), a characteristic peak with a 397.10 eV binding energy is observed in the N regions. It is attributed to metal-nitrogen bonds, indicating the presence of zero-valent N (0) atoms in the N-B-Ni_5Fe_5P/SEP and N, B-NiP/ SEP (Fig. 5d). The presence of N dopant in the sample will inherently improve the interaction ability with the reactants and produce a higher positive charge density on its adjacent carbon atoms, which may also contribute to the high activity of the sample (Sun et al., 2020). Therefore, the above results indicate that the zero-valent N and B atoms were successfully doped into N, B-NiP/SEP and N-B-Ni_5Fe_5P/SEP.

The crystallization and graphitization degree of the carbonized SEP support on the Ni-supported catalyst and Ni-Fe bimetallic catalyst were studied by Raman spectroscopy. In general, an I_D/I_G ratio less than one is ideal. As shown in Fig. 6, the carbon fibre carriers have high quality and crystallinity, and the peak intensity ratio (I_D/I_G) is less than one, and the spectra of carbon samples show two distinct bands. The first band is the well-known D band, located at 1363 cm^{-1}, attributed to the disorder in the carbon structure, such as defects in the carbon structure or amorphous carbon (Msda et al., 2002; Awadallah et al., 2013). The vibration of sp2 carbon atoms in the graphitization region forms the G band located at 1589 cm^{-1} (Ali et al., 2017; Allaedini et al., 2015). Generally, the ratio of the D-band strength to G-band strength I_D/I_G is used to reflect the degree of graphitization. The I_D/I_G ratio of N-B-Ni_5Fe_5P/SEP is 0.89, which indicates that a large number of defects and irregular structures were introduced into the carbon fiber carrier. The I_D/I_G ratio further increased to 0.95 for N-B-NiP/SEP, indicating the enhanced number of structural defects, increased localized sp3 defects in sp2 framework and high electrical conductivity.

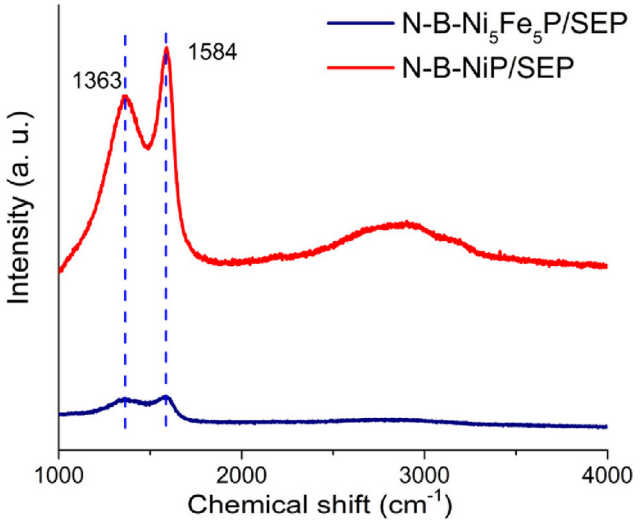

Fig. 6 Raman spectra of N-B-Ni_5Fe_5P/SEP and N-B-NiP/SEP.

The specific surface area and porosity of the obtained materials were investigated by N_2 adsorption–desorption experiments. In the curves of N-B-Ni_5Fe_5P/SEP and N-B-NiP/SEP (Fig. 7a), the type IV adsorption branches corresponded to the mesoporous structure. According to IUPAC classification, the isotherms (Fig. 7) of the mixed oxides were classified as type IV with an H_3 hysteresis loop, suggesting the existence of mesoporous materials with an incision-like pore geometry. The specific surface area of N-B-Ni_5Fe_5P/SEP and N-B-NiP/SEP were calculated to be 55.44 and 57.18 m^2/g, respectively. The pore size distributions are shown in Fig. 7b. The average pore size of N-B-Ni_5Fe_5P/SEP was about 11.86 nm, while those of N-B-NiP/SEP was around 8.42 nm. It was clear that N-B-Ni_5Fe_5P/SEP and N-B-NiP/SEP were mainly composed of micropores and mesopores of size around 10 nm. As shown in Fig. 7d, the average pore widths of two samples follow the order of N-B-Ni_5Fe_5P/SEP > N-B-NiP/SEP and the pore volumes of N-B-Ni_5Fe_5P/SEP and N-B-NiP/SEP were 0.19 and 0.11 cm^3/g, respectively. The pore structure of materials play an important and even decisive role in determining many material properties. When using carbon materials as carriers, their porous properties are conducive to the diffusion of substrates and products and can lead to the exposure of more active sites, thus improving the overall activity of the catalyst.

8. Catalytic performance

8.1. Oxygen evolution reaction

The electrocatalytic OER performance of N-B-Ni_5Fe_5P/SEP and N-B-NiP/SEP were studied in O_2-saturated 1 M KOH. The LSV data (Fig. 8a-b) were recorded with the scan rate of 5 mV/s. For N-B-NiP/SEP, the Ni^{2+}/Ni^{3+} was oxidized in the potential range of 1.35–1.5 V (all potentials were versus the RHE) (Fig. 8b). The presence of the oxidation peak indicated that because of insufficient oxidation, a fully protected NiO shell may not be formed outside the Ni nanoparticles, leading to corrosion of metal Ni and the formation of NiOOH during OER in the alkaline solution (Sivanantham et al., 2016). The curves of polarization (Fig. 8a-b) showed that the N-B-Ni_5Fe_5P/SEP exhibited excellent OER performance with an overpotential of 395 mV at 10 mA/cm^2 and 488 mV at 30 mA/cm^2 current density, compared to N-B-NiP/SEP (431 and 579 mV, respectively).

In addition, to investigate the kinetics of these catalysts, the Tafel slopes obtained from the LSV polarization curves are shown in Fig. 8c. The Tafel slope of N-B-Ni_5Fe_5P/SEP (101 mV/dec) was considerably smaller than that of N-B-NiP/SEP (151 mV/dec), confirming the faster OER kinetics

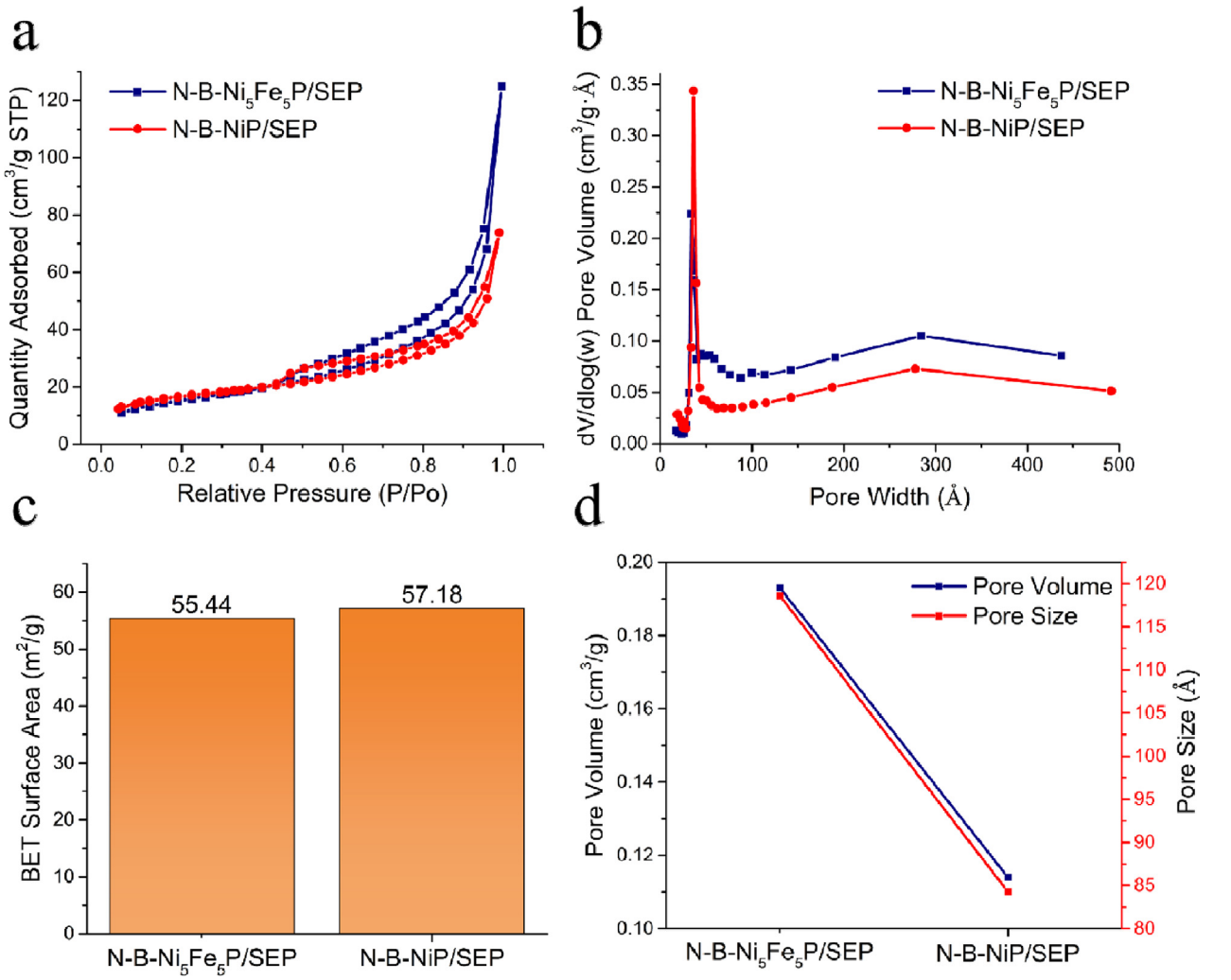

Fig. 7 N_2 adsorption-desorption curves (a), pore distribution curve (b), specific surface area (c), Pore volume and pore diameter (d) of N-B-Ni_5Fe_5P/SEP and N-B-NiP/SEP.

of the former. Our research results indicate that the synergetic effect of the Ni-Fe bimetal loading and carbon carrier played an important role in facilitating the OER kinetics (Li et al., 2020; Jiang et al., 2018; Yue et al., 2019).

8.2. Hydrogen evolution reaction

To assess the electrocatalytic HER activity of the N-B-Ni_5Fe_5P/SEP and N-B-NiP/SEP, the related electrochemical measurements were performed using a three-electrode system. Fig. 8d shows the polarization curves of the N-B-Ni_5Fe_5P/SEP and N-B-NiP/SEP in N_2-saturated 0.5 M H_2SO_4 solution. While the N-B-NiP/SEP, which has a η10 value of 397 mV, the N-B-Ni_5Fe_5P/SEP requires 392 mV to reach 10 mA/cm^2, implying that the Fe trace in N-B-Ni_5Fe_5P/SEP does not contribute to the electrochemical activities and remains a mere spectator species. Tafel slopes were drawn to evaluate HER kinetics (Fig. 8e). The Tafel slope is 122 mV/dec for N-B-Ni_5Fe_5P/SEP, which is much smaller than that of the N-B-NiP/SEP (119 mV/dec). In the study of the mechanism of electrocatalytic hydrogen evolution in acidic media, it is generally believed that the reaction process is divided into the following three steps: the first step is the electrochemical reaction process; the second step is the electrochemical desorption process; the third step is the compound desorption process. The general HER mechanism includes at least an electrochemical process and a desorption process, and hence, it can be divided into the Volmer-Heyrovsky mechanism or Volmer-Tafel mechanism according to the different rate steps. As seen from Fig. 8c and e, the Tafel slopes of the N-B-Ni_5Fe_5P/SEP and N-B-NiP/SEP are 122 and 119 mV/dec, respectively. So the hydrogen evolution process of the catalyst in acidic medium is a slow discharge mechanism, and the Volmer reaction process has a rate-control step, which is the Volmer-Heyrovsky mechanism (Conway and Tilak, 2002; Li et al., 2014; Li et al., 2011).

8.3. Catalytic activity for 4-NP hydrogenation as a model reaction

The removal of 4-NP from wastewater is of significant importance from the perspective of environment protection as 4-NP is a prevalent contaminant produced in industry and agriculture (Choi and Oh, 2019; Ding et al., 2020). It is known that

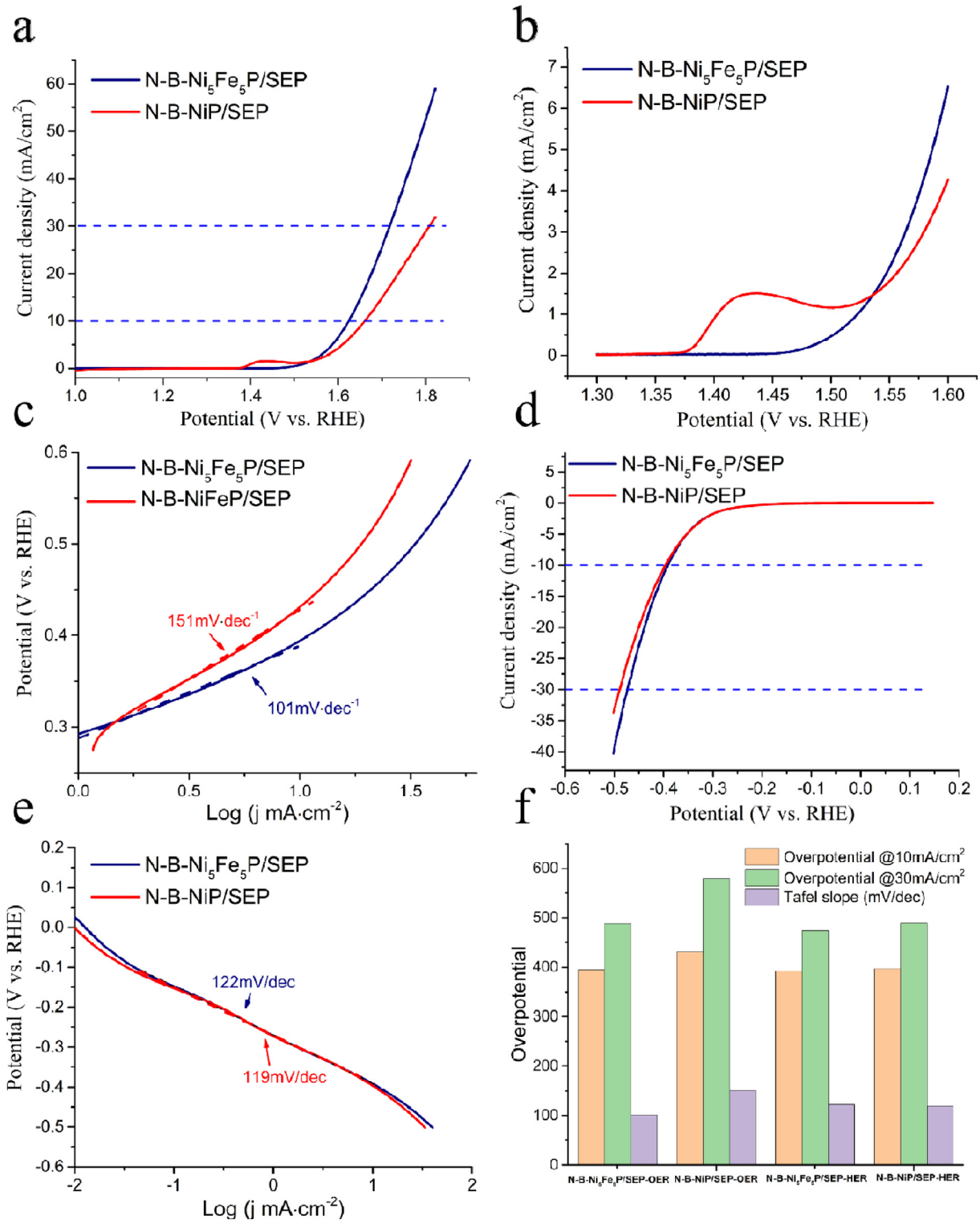

Fig. 8 Electrochemical performance in acid and basic solution. (a) polarization curves for OER. (b) polarization curves (1.3–1.5 V) for OER. (c) Tafel plots for OER. (d) polarization curves for HER. (e) Tafel plots for HER. (f) Overpotential for HER and OER.

4-aminophenol (4-AP) is very useful and important in many applications, and it is used in analgesic and antipyretic drugs, photographic developer, corrosion inhibitors and anticorrosion lubricants. The reduction of 4-NP to 4-AP has been extensively used as a benchmark system to evaluate the catalytic activity of metal NPs (Chang et al., 2012; Yang et al., 2014).

Therefore, the reduction of 4-NP toward 4-AP in the presence of $NaBH_4$ was selected as a model reaction to further con-

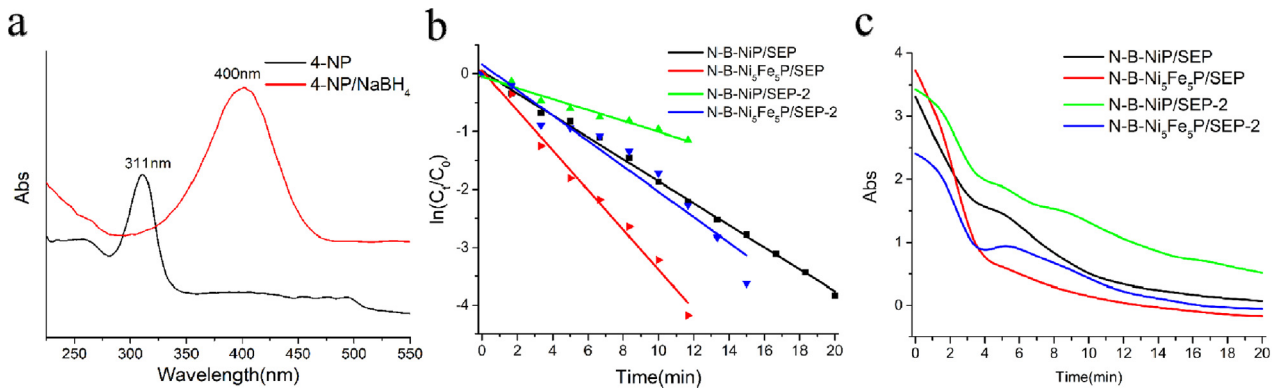

Fig. 9 (a) UV–vis spectra of 4-nitrophenol before and after adding $NaBH_4$ solution, (b) the relationship between $\ln(C_t/C_0)$ and reaction time (t), (c) the reduction of 4-nitrophenol in aqueous solution recorded with time using 3.0 mg N-B-Ni_5Fe_5P/SEP and N-B-NiP/SEP.

firm the generality of the N-B-Ni_5Fe_5P/SEP and N-B-NiP/SEP. As shown in Fig. 9a, the adsorption peak of 4-NP was red-shifted from 317 to 400 nm immediately upon the addition of $NaBH_4$ solution which corresponds to a colour change from light yellow to yellow green because of the formation of the 4-nitrophenolate ion under alkaline conditions. When the catalyst was added, the intensity of the characteristic peak at 400 nm rapidly declined. The reduction of 4-NP was completed within 10 min over 10 mg N-B-NiP/SEP and N-B-Ni_5Fe_5P/SEP (Fig. 9c). Considering that the reductant concentration is much higher than that of 4-NP ($C_{NaBH4}/C_{4\text{-}NP}$ = 100) in the reaction mixture, the pseudo-first-order rate kinetics with respect to 4-NP concentration could be used to evaluate the catalytic rate. The reaction kinetics can be described as $-\ln(C_t/C_0) = kt$, where k is the rate constant at a given temperature and t is the reaction time. C_0 and C_t are the 4-NP concentration at the beginning and at time t, respectively. As expected, a good linear correlation of $\ln(C_t/C_0)$ vs. reaction time t was obtained (Fig. 9b), and the kinetic rate constant k was estimated as 0.19 (R^2 = 0.99) and 0.344 (R^2 = 0.99) min^{-1} for N-B-NiP/SEP and N-B-Ni_5Fe_5P/SEP, respectively. To compare different catalysts, we calculated the ratio of rate constant K over the total weight of the nickel catalyst, where K = k/m. Thus the activity factor K was calculated as 19 and 34.4 $min^{-1}\cdot g^{-1}$ for N-B-NiP/SEP and N-B-Ni_5Fe_5P/SEP, respectively. It is clear that N-B-Ni_5Fe_5P/SEP clearly had the largest activity factor, compared with other precious metal catalysts such as Ru/C (0.034 min^{-1}) and Ru/PC-IM (0.198 min^{-1}) (Ding et al., 2020). With an increase in the number of cycles, the conversion of 4-NP decreased slightly, possibly because of the partial loss of active surface area caused by the partial loss of catalyst during recovery.

The excellent catalytic performances of N-B-Ni_5Fe_5P/SEP for 4-NP reduction lead to the following advantages. From the point of view of catalysis, SEP is an ideal substrate for the growth of an active catalyst layer. Because there are abundant coordination hydroxyl groups and epoxy functional groups on the cellulose microfiber, the ultra-fine and clean metal nanoparticles formed in situ are uniformly dispersed on the surface of the carrier rather than being embedded in the carrier. Together, these two functions can lead to stronger binding and faster mass transfer kinetics.

9. Conclusions

In summary, using economical and recyclable fiber raw materials as carriers, nickel-supported catalysts were prepared by adsorption and reduction at room temperature. For the model catalytic hydrogenation of 4-NP by $NaBH_4$, the N-B-NiP/SEP and N-B-Ni_5Fe_5P/SEP catalysts exhibited much better catalytic performances than the other catalysts recently reported in terms of the catalytic activity (with the proposed catalysts, the reaction was completed within 10 min) and reaction rate constant (0.19 and 0.344 min^{-1} for N-B-NiP/SEP and N-B-Ni_5Fe_5P/SEP catalysts, respectively). The catalyst showed activities for electrocatalytic HER and OER under ambient conditions. In general, the reported preparation method of nickel-supported catalyst is convenient, economical and environment-friendly, which is in agreement with many green chemistry and sustainable development principles, and the method employs widely available starting materials.

Acknowledgements

The authors are grateful for the support of the National Nature Science Foundation of China (NSFC, No. 21978074).

References

Awadallah, A.E., Aboul-Enein, A.A., Aboul-Gheit, A.K., 2013. Various nickel doping in commercial Ni-Mo/Al_2O_3 as catalysts for natural gas decomposition to COx-free hydrogen production. Renwable Energy. 57, 671–678.

Allaedini, G., Aminayi, P., Tasirin, S.M., 2015. The effect of alumina and magnesia supported germanium nanoparticles on the growth of carbon nanotubes in the chemical vapor deposition method. J. Nanomater., 1–6

Ali, B., Dayang, R.A.B., Sapuan, S.M., et al, 2017. Preparation of carbon nanotubes via chemical technique (modified staudenmaier method). Nanosci. Nanotechnol.-Asia 7 (1), 113–122.

Anjum, M.A.R., Okyay, M.S., Kim, M., et al, 2018. Bifunctional sulfur-doped cobalt phosphide electrocatalyst outperforms all-noble-metal electrocatalysts in alkaline electrolyzer for overall water splitting. Nano Energy 53, 286–295.

Conway, B.E., Tilak, B.V., 2002. Interfacial processes involving electrocatalytic evolution and oxidation of H_2, and the role of chemisorbed H. Electrochim. Acta 47 (22), 3571–3594.

Coates J., 2006. Interpretation of Infrared Spectra, A Practical Approach. Encyclopedia of analytical chemistry.

Chang, G., Luo, Y., Lu, W., et al, 2012. Ag nanoparticles decorated polyaniline nanofibers: synthesis, characterization, and applications toward catalytic reduction of 4-nitrophenol and electrochemical detection of H_2O_2 and glucose. Catal. Sci. Technol. 2 (4), 800–806.

Chang, J.F., Xiao, Y., Luo, Z.Y., et al, 2016. Recent progress of non-noble metal catalysts in water electrolysis for hydrogen production. Acta Phys. Chim. Sin. 32 (7).

Choi, S., Oh, M., 2019. Well-arranged and confined incorporation of PdCo nanoparticles within a hollow and porous metal-organic framework for superior catalytic activity. Angew. Chem. Int. Ed. 58 (3), 866–871.

Cao, Y.Q., Zhang, H., Ji, S.F., et al, 2020. Adsorption site regulation to guide atomic design of Ni-Ga catalysts for acetylene semi-hydrogenation. Angewandte Chemie-International Edition. 59 (28), 11647–11652.

Ding, Y., Miao, B.Q., Li, S.N., et al, 2020a. Benzylamine oxidation boosted electrochemical water-splitting: Hydrogen and benzonitrile co-production at ultra-thin NiP nanomeshes grown on nickel foam. Appl. Catal. B-Environ. 268, 118393.

Ding, R., Chen, Q., Luo, Q., et al, 2020b. Salt template-assisted in situ construction of Ru nanoclusters and porous carbon: excellent catalysts toward hydrogen evolution, ammonia-borane hydrolysis, and 4-nitrophenol reduction. Green Chem. 22 (3), 835–842.

Fu Y.K., Qin L., Huang D.L., et al., 2019a. Chitosan functionalized activated coke for Au nanoparticles anchoring: Green synthesis and catalytic activities in hydrogenation of nitrophenols and azo dyes. Appl. Catal. B-Environ., 255.

Foroutan, F., Carta, D., McGuire, J., et al, 2019. Antibacterial copper-doped calcium phosphate glasses for bone tissue regeneration. ACS Biomater. Sci. Eng. 5, 6054–6062.

Hao, J.H., Yang, W.S., Peng, Z., et al, 2017. A Nitrogen doping method for CoS_2 electrocatalysts with enhanced water oxidation performance. ACS Catal. 7 (6), 4214–4220.

Jiang S.f., Yi B.L., Zhao Q., et al., 2017. Palladium-nickel catalysts based on ordered titanium dioxide nanorod arrays with high catalytic peformance for formic acid electro-oxidation. RSC Adv. 7 (19), 11719–11723.

Jiang, J., Sun, F.F., Zhou, S., et al, 2018. Atomic-level insight into super-efficient electrocatalytic oxygen evolution on iron and vanadium co-doped nickel (oxy)hydroxide. Nat. Commun. 9 (2885).

Jiao, S.L., Yao, Z.Y., Li, M.F., et al, 2019. Accelerating oxygen evolution electrocatalysis of two-dimensional NiFe layered double hydroxide nanosheets via space-confined amorphization. Nanoscale. 11 (40), 18894–18899.

Kuo, M.Y., Hsiao, C.F., Chiu, Y.H., et al, 2019. Au@Cu2O core@shell nanocrystals as dual-functional catalysts for sustainable environmental applications. Appl. Catal. B: Environ. 242, 499–506.

Kümmerer, K., Clark, J.H., Zuin, V.G., 2020. Rethinking chemistry for a circular economy. Science 367 (6476), 369–370.

Kim, S.H., Park, Y.S., Kim, C., et al, 2020. Self-assembly of Ni-Fe layered double hydroxide at room temperature for oxygen evolution reaction. Energy Rep. 6, 248–254.

Li, Y.G., Wang, H.L., Xie, L.M., et al, 2011. MoS_2 nanoparticles grown on graphene: an advanced catalyst for the hydrogen evolution reaction. J. Am. Chem. Soc. 133 (19), 7296–7299.

Li, D.J., Maiti, U.N., Lim, J., et al, 2014. Molybdenum sulfide/N-doped CNT forest hybrid catalysts for high-performance hydrogen evolution reaction. Nano Lett. 14 (3), 1228–1233.

Lai, C., Zhang, M., Li, B., et al, 2019. Fabrication of CuS/$BiVO_4$ (0 4 0) binary heterojunction photocatalysts with enhanced photocatalytic activity for Ciprofloxacin degradation and mechanism insight. Chem. Eng. J. 358, 891–902.

Lan, K., Li, J., Zhu, Y., et al, 2019. Morphology engineering of $CoSe_2$ as efficient electrocatalyst for water splitting. J. Colloid Interface Sci. 539, 646–653.

Lee, S., Cho, H.S., Cho, W.C., et al, 2019. Operational durability of three-dimensional Ni-Fe layered double hydroxide electrocatalyst for water oxidation. Electrochim. Acta 315, 94–101.

Li, Y.Y., Huang, J.W., Rao, G.F., et al, 2020. Enhanced water oxidation activity of 3D porous carbon by incorporation of heterogeneous Ni/NiO nanoparticles. Appl. Surface Sci. 530.

Msda, B., Gd, C., Ajb, D., et al, 2002. Raman spectroscopy on isolated single wall carbon nanotubes. Carbon 40 (12), 2043–2061.

Mansouriieh, N., Sohrabi, M.R., Khosravi, M., 2016. Adsorption kinetics and thermodynamics of organophosphorus profenofos pesticide onto Fe/Ni bimetallic nanoparticles. Int. J. Environ. Sci. Technol. 13 (5), 1393–1404.

Mitchell, S.W.L., Thomas, C.K.Y., JoyceTiong, T., et al, 2021. Ultrasound-assisted sequentially precipitated nickel-silica catalysts and its application in the partial hydrogenation of edible oil. Ultrason. Sonochem. 73, 105490.

Pinilla, J.L., de, L.S., Moliner, R., et al., 2016. Ni-Co bimetallic catalysts for the simultaneous production of carbon nanofibres and syngas through biogas decomposition. Appl. Catal. B-Environ. 200, 255–264.

Sivanantham, A., Ganesan, P., Shanmugam, S., 2016. Hierarchical NiCo2S4 nanowire arrays supported on Ni foam: an efficient and durable bifunctional electrocatalyst for oxygen and hydrogen evolution reactions. Adv. Funct. Mater. 26 (26), 4661–4672.

Sahasrabudhe, A., Dixit, H., Majee, R., et al, 2018. Value added transformation of ubiquitous substrates into highly efficient and flexible electrodes for water splitting. Nat. Commun. 9 (2014).

Sung, J.b., Wang, H.Y., Zhang, D., et al., 2018. Confined-interface-directed synthesis of Palladium single-atom catalysts on graphene/amorphous carbon. Appl. Catal. B. Environ. 225, 291–297.

Sun, Y.Q., Xu, K., Zhao, Z.H., et al, 2020. Strongly coupled dual zerovalent nonmetal doped nickel phosphide nanoparticles/N, B-graphene hybrid for pH-Universal hydrogen evolution catalysis. Appl. Catal. B-Environ. 278 (119284).

Xiao, C.L., Li, Y.B., Lu, X.Y., et al, 2016. Bifunctional porous NiFe/$NiCo_2O_4$/Ni foam electrodes with triple hierarchy and double synergies for efficient whole cell water splitting. Adv. Funct. Mater. 26 (20), 3515–3523.

Xu, K., Ding, H., Zhang, M.X., et al, 2017. Regulating water-reduction kinetics in cobalt phosphide for enhancing HER catalytic activity in alkaline solution. Adv. Mater. 29 (28).

Xu, W.J., Lyu, F.L., Bai, Y.C., et al, 2018. Porous cobalt oxide nanoplates enriched with oxygen vacancies for oxygen evolution reaction. Nano Energy 43, 110–116.

Yang, Y., Ren, Y., Sun, C.J., Hao, S.J., 2014. Facile route fabrication of nickel based mesoporous carbons with high catalytic performance towards 4-nitrophenol reduction. Green Chem.. 16 (4), 2273–2280.

Yang, H., Wang, C., Zhang, Y., et al, 2019. Green synthesis of NiFe LDH/Ni foam at room temperature for highly efficient electrocatalytic oxygen evolution reaction. Sci. China Mater. 62 (5), 681–689.

Yue, S., Wang, S.S., Jiao, Q.Z., et al, 2019. Preparation of yolk-shell-structured CoxFe1-xP with enhanced OER performance. ChemSusChem 12 (19), 4461–4470.

Yusuf, M., Farooqi, A.S., Ying, Y.X., et al, 2021. Synthesegasherstellung unter Verwendung von Nickel auf Aluminium-Magnesium unterstütztem Katalysator durch Trockenreformierung von Methan. Mater. Sci. Eng. Technol. 52 (10), 1090–1100.

Zhou, C., Lai, C., Zhang, C., et al, 2018. Semiconductor/boron nitride composites: synthesis, properties, and photocatalysis applications. Appl. Catal. B 238, 6–18.